Millimeter-Wave Four-Wave Mixing via Kinetic Inductance for Quantum Devices

Alexander Anferov,[1,2,*] Aziza Suleymanzade,[1,2] Andrew Oriani,[2,3] Jonathan Simon,[1,2,3] and David I. Schuster[1,2,3,†]

[1] *James Franck Institute, University of Chicago, Chicago, Illinois 60637, USA*
[2] *Department of Physics, University of Chicago, Chicago, Illinois 60637, USA*
[3] *Pritzker School of Molecular Engineering, University of Chicago, Chicago, Illinois 60637, USA*

(Received 6 September 2019; revised manuscript received 11 December 2019; accepted 9 January 2020; published 21 February 2020)

Millimeter-wave superconducting devices offer a platform for quantum experiments at temperatures above 1 K, and new avenues for studying light-matter interactions in the strong coupling regime. Using the intrinsic nonlinearity associated with kinetic inductance of thin-film materials, we realize four-wave mixing at millimeter-wave frequencies, demonstrating a key component for superconducting quantum systems. We report on the performance of niobium nitride resonators around 100 GHz, patterned on thin (20–50-nm) films grown by atomic layer deposition, with sheet inductances up to 212 pH/□ and critical temperatures up to 13.9 K. For films thicker than 20 nm, we measure quality factors from 1×10^4 to 6×10^4, and explore potential loss mechanisms. Finally, we measure degenerate parametric conversion for a 95-GHz device with a forward efficiency up to +16 dB, paving the way for the development of nonlinear quantum devices at millimeter-wave frequencies.

DOI: 10.1103/PhysRevApplied.13.024056

I. INTRODUCTION

For superconducting quantum circuits, the millimeter-wave spectrum presents a fascinating frequency regime between microwaves and visible light, giving access to a wider range of energy scales and lower sensitivity to thermal background noise due to higher photon energies. Many advances have been made in refining microwave quantum devices [1,2], typically relying on ultralow temperatures in the millikelvin range to reduce sources of noise and quantum decoherence. Use of millimeter-wave photons as building blocks for superconducting quantum devices offers transformative opportunities by allowing quantum experiments to be run at liquid-helium-4 temperatures, allowing higher device power dissipation and enabling large-scale direct integration with semiconductor devices [2]. Millimeter-wave quantum devices could also provide new routes for studying strong-coupling light-matter interactions in this frequency regime [3–7] and present new opportunities for quantum-limited frequency conversion and detection [8,9].

Recent interest in next-generation communication devices [10,11] has led to important advances in sensitive millimeter-wave measurement technology around 100 GHz. Realizing quantum systems at these frequencies, however, requires both low-loss components—device materials with low absorption rates [12–14] and resonators with long photon lifetimes [15–20]—and most importantly, elements providing nonlinear interactions, which for circuit quantum optics can be realized with four-wave-mixing Kerr terms in the Hamiltonian. One approach commonly used at microwave frequencies relies on aluminum Josephson junctions [2], which yield the necessary four-wave mixing at low powers. However, to avoid breaking Cooper pairs with high-frequency photons, devices at millimeter-wave frequencies are limited to materials with higher superconducting critical temperatures (T_c). Higher-T_c junctions have been implemented as high-frequency mixers for millimeter-wave detection [9,21,22], and ongoing efforts are decreasing losses for quantum applications [23,24].

Kinetic inductance (KI) offers a promising alternative source of Kerr nonlinearity arising from the inertia of Cooper pairs in a superconductor, has gained interest recently for microwave quantum applications [25,26], and has also been successfully used for millimeter-wave detection [27,28]. Niobium nitride (NbN) is an ideal material for KI, as it has a high intrinsic sheet inductance [29–31], a relatively high T_c between 14 and 18 K [29–32] making it suitable for high-frequency applications [14], and good microwave-loss properties [33]. Among deposition methods, atomic layer deposition (ALD) offers conformal growth of NbN [32] and promising avenues

*aanferov@uchicago.edu
†david.schuster@uchicago.edu

for realizing repeatable high-KI devices on a wafer scale [25].

In this work, we explore kinetic inductance as a nonlinear element for quantum devices at millimeter-wave frequencies using high-KI resonators in the W band (75–110 GHz) fabricated from thin films of NbN deposited via ALD. We study potential loss mechanisms at powers down to single-photon occupations. Using the power-dependent frequency shift, we characterize the nonlinearity arising from KI, the strength of which varies with wire width and material properties. With two-tone spectroscopy, we observe degenerate four-wave mixing near single-photon powers. These measurements demonstrate the necessary core components for millimeter-wave circuit quantum optics, paving the way for a new generation of high-frequency high-temperature experiments.

II. MEASUREMENT METHODS

We investigate properties of millimeter-wave high-KI resonators in the quantum regime (at temperatures of 1 K) in a helium-4 adsorption refrigerator. Using a frequency multiplier, cryogenic mixer, and low-noise amplifier, we measure the complex transmission response as shown in Fig. 1(a). Input attenuation reduces thermal noise reaching the sample, enabling transmission measurements in the single-photon limit set by the thermal background. Rectangular waveguides couple the signal in and out of a 200-μm-deep slot, the dimensions of which are carefully selected to shift spurious lossy resonances out of the W band. To reduce potential conductivity losses, the waveguide and the slot are coated with 200 nm of evaporated niobium. Below 9 K, this helps shield the sample from stray magnetic fields; however, devices with higher T_c are not shielded from magnetic fields while cooling through their superconducting transition. We use indium to mount a chip patterned with six resonators in the slot, as shown in Fig. 1(b). Devices are patterned on 100-μm-thick sapphire, which has low dielectric loss and minimizes spurious substrate resonances in the frequency band of interest. The planar resonator geometry shown in Fig. 1(c) consists of a shorted quarter-wave section of a balanced-mode coplanar stripline waveguide (CPS), which couples directly to the TE_{10} waveguide through dipole radiation, which we enhance with dipole antennas. We find that this design is well described by the analytic model presented in Ref. [34], which takes into account the thin-film linear kinetic inductance. For very thin or narrow wire widths, the total inductance is dominantly kinetic, making the resonators extremely sensitive to superconducting-film properties.

III. MATERIALS AND LOSS MECHANISMS

To understand the quality of the NbN films grown by ALD and accurately predict resonant frequencies, we characterize material properties with dc electrical measurements. All devices in this work are deposited on sapphire with a process based that desribed in Ref. [32], and etched with a fluorine-based inductively coupled plasma (See Appendix B). We measure resistivity at ambient magnetic fields as a function of temperature (See Appendix C), which we use to extract T_c for a range of film thicknesses [see Fig. 2(a)]. The inset in Fig. 2(a) shows that our films follow a universal relation observed for thin superconducting films [29] linking T_c, film thickness t, and sheet resistance $R_\square$: we find that our results are similar to those for NbN deposited with other methods [29,31]. For thicker films, T_c appears to saturate at 13.8–13.9 K, which is comparable to what was found in other studies [29,30,32], while decreasing to 8.7 K for the thinnest film ($t = 7$ nm), which can be attributed to disorder-enhanced Coulomb repulsions [35,36]. We also find that the superconducting transition width increases greatly for the thinner films, which can in turn be attributed to a disorder-broadened density of states [36] or reduced vortex-antivortex pairing energies at the transition [33,37].

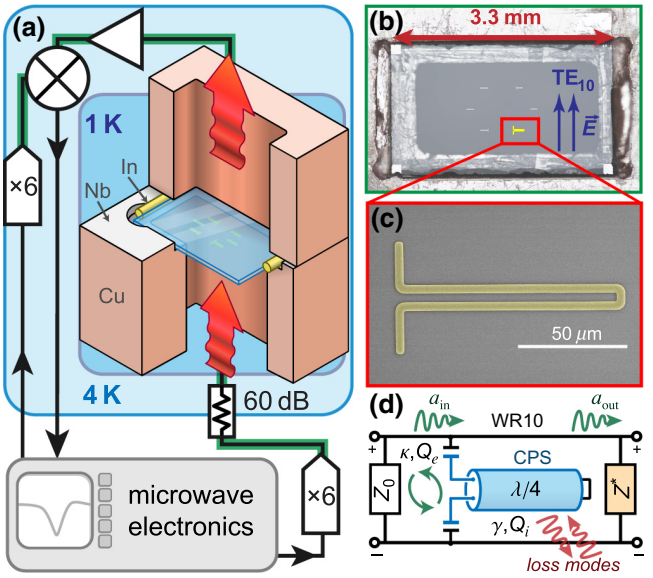

FIG. 1. Device characterization and design. (a) Sixfold frequency multipliers convert microwave signals to millimeter-wave signals (green), which are demodulated with a cryogenic mixer. A cutaway shows copper WR10 rectangular waveguides coupling the signal in and out of a Nb-coated slot, into which we mount a chip patterned with six resonators. (b) Top-down composite micrograph showing a mounted chip with the top waveguide removed. (c) Scanning electron micrograph of a typical resonator used in this work, with wire width $w = 4$ μm and film thickness $t = 27.8$ nm (NbN false-colored yellow). Dipole-coupling antennas extend on the left of the quarter-wave resonator. Measurements can be described with input and loss couplings Q_e and Q_i with use of the circuit model in (d), which takes into account the impedance mismatch between the waveguide Z_0 and the slot with a sapphire chip Z^*.

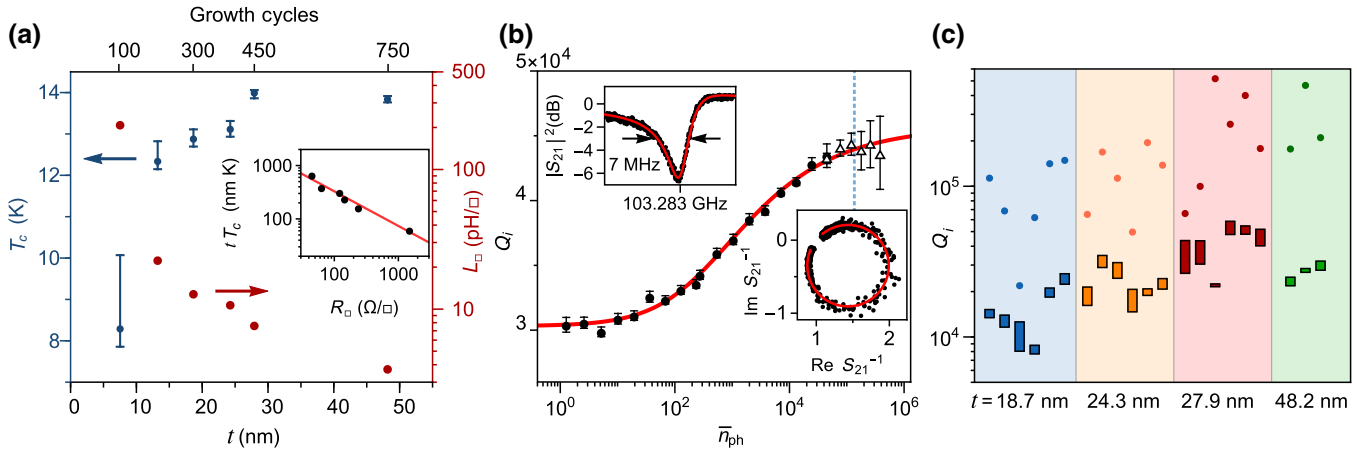

FIG. 2. Material and loss characterization. (a) Superconducting critical temperature (T_c) and sheet inductance ($L_\square$) of deposited NbN as a function of film thickness (t). Bars denote temperatures corresponding to 90% and 10% reductions from the maximum resistivity. The inset shows the dependence of tT_c on $R_\square$ with a fit (red) to $tT_c = AR_\square^{-B}$, where $A = 6487 \pm 1607$ and $B = 0.647 \pm 0.05$ (b) Power dependence of the internal quality factor for a resonator with $Q_e^* = 2.759 \times 10^4$ patterned on a 27.9-nm-thick NbN film measured at 1 K. White triangles are fits to a nonlinear-response model near and above the bifurcation power (dashed line). The red line is a fit to a model including power-dependent loss from two-level systems, and power-independent loss. The insets show the lineshape and fits at average photon occupation $\bar{n}_{ph} \approx 1.2$. (c) Internal quality factors for resonators in this study, grouped by film thickness. The top and bottom of the colored bars correspond to fitted low-power and high-power saturation values, while points correspond to two-level-system-induced Q_i with high-power loss subtracted.

From the resistivity and critical temperature, we determine the sheet inductance $L_\square = \hbar R_\square / \pi \Delta_0$, where the normal sheet resistance $R_\square = \rho_n / t$ is taken as the maximum value of normal resistivity ρ_n, occurring just above T_c, and $\Delta_0 = 2.08 T_c$ is the superconducting energy gap predicted by Bardeen-Cooper-Schrieffer (BCS) theory for NbN [30,33]. We observe a monotonic increase in $L_\square$ for thinner films, achieving a maximum $L_\square = 212$ pH/□, comparable to that for similar high-KI films [25,38].

By characterizing complex transmission spectra of resonators fabricated on a range of film thicknesses, we explore loss mechanisms at millimeter-wave frequencies. The sheet inductance, thickness, and T_c measured for a given film are used to adjust the resonator design length. This spreads resonances out in frequency from 80 to 110 GHz, while varying antenna lengths allows us to adjust coupling strengths. A typical normalized transmission spectrum taken at single-photon-occupation powers ($\bar{n}_{ph} \approx 1.2$) is shown in the inset in Fig. 2(b). On resonance, we observe a dip in magnitude, which at low powers is described well by [39]

$$S_{21} = 1 - \frac{Q}{Q_e^*} \frac{e^{i\phi}}{1 + 2iQ\frac{\omega - \omega_0}{\omega_0}}, \tag{1}$$

where $Q^{-1} = Q_i^{-1} + \mathrm{Re}\, Q_e^{-1}$ [39] and the coupling quality factor $Q_e = Q_e^* e^{-i\phi}$ has undergone a complex rotation ϕ due to an impedance mismatch [39,40], likely induced by the sapphire chip and slot altering the waveguide geometry. The plot of fitted internal quality factors with respect to photon occupation in Fig. 2(b) shows that Q_i increases with power. This can be described by a power-dependent saturation mechanism [41,42], likely originating from two-level systems (TLS) in the slow-growing amorphous surface oxide [43]. At high powers, Q_i approaches a limit, indicating that another power-independent loss mechanism, such as dielectric or radiative loss, is dominant in this regime. For some samples, this limit is obscured by the early onset of nonlinear effects (see Appendix E for the discussion of temperature-dependent loss mechanisms).

To study effects of film thickness on Q_i, we repeat the measurements summarized in Fig. 2(b) for devices ranging in thickness from 19.5 to 48.8 nm and show the results in Fig. 2(c). We plot the low-power and high-power limits of Q_i as well as a lower bound for the TLS-induced Q_i for devices from six separate chips grouped by film thickness. For films thicker than 20 nm, we consistently find $Q_i > 10^4$, with the TLS limiting Q_i around 10^5. We find a weak correlation of Q_i with film thickness, which could be explained by several additional potential sources of loss. Thinner films exhibiting higher disorder have also been connected with a nonlinear resistance [44], resulting in loss mechanisms proportional to kinetic inductance (see Appendix F). Additionally, since the devices are unshielded from ambient magnetic fields at the superconducting transition, vortices trapped in the thin films may cause additional dissipation [33,37,45,46] dependent on film thickness. Resonances patterned from thinner films proved experimentally difficult to distinguish from background fluctuations, possibly indicating

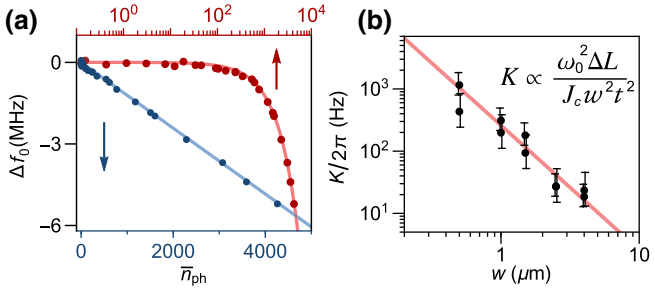

FIG. 3. Measuring Kerr nonlinearity. (a) Frequency shift versus average resonator photon number $\bar{n}_{ph}$ on a linear and a log scale ($\bar{n}_{ph}$ accurate within a factor of approximately 10). (b) Extracted self-Kerr-coefficients versus wire width w for resonators fabricated from a 29-nm-thick film. The predicted w^{-2} dependence is shown in red. We find no significant impact of w on Q_i.

low values of Q_i or frequencies outside the measurement bandwidth.

IV. KERR NONLINEAR DYNAMICS

A key aspect of high-KI resonators is their fourth-order nonlinearity, an important component for realizing quantum devices, and similar to the nonlinearity term found in Josephson junctions for low powers. Nonlinear kinetic inductance takes the general form $L = L_k + \Delta L_k I^2/I_c^2$, where L_k is the linear kinetic inductance, ΔL_k is the nonlinear kinetic inductance, and I_c is the critical current, which sets the nonlinearity scale [44,47]. This adds nonlinear terms of the form $(\hbar/2)K(a^\dagger a)^2$ to the Hamiltonian, with $K \propto \omega_0^2 \Delta L_k/I_c^2$, shifting the fundamental frequency ω_0 by the self-Kerr-constant K for each photon added. To characterize the strength of the resonator nonlinearity, we measure the resonance-frequency shift [48] as a function of photon number [49]. A linear fit for a resonator ($t = 29$ nm, $w = 0.5$ μm) yielding $K/2\pi = 1.21$ kHz is shown in Fig. 3(a). Although the statistical errors of the fits are small, we note this value has a multiplicative uncertainty of $10^{\pm 0.4}$: despite careful calibration, systematic variations in received power across the chip and between separate experiments limit the best estimates of photon number to within a factor of approximately 10. By writing the self-Kerr-coefficient in terms of a current density $I_c = J_c wt$, we expect K to scale as w^{-2}, so in Fig. 3(b) we plot the self-Kerr-coefficients of the devices (and error relative to each other) with respect to their wire width. These results are comparable to self-Kerr-strengths of granular aluminum nanowires [49] or weakly nonlinear Josephson junctions [50].

A hallmark of Kerr nonlinearity is the distortion of the transmission lineshape in frequency space at high powers, ultimately leading to a multivalued response above the bifurcation power. If we rewrite $\gamma = \omega_0/Q_i$ and $\kappa = \omega_0/\mathrm{Re}\, Q_e$, the steady-state nonlinear response takes the form derived from Refs. [44,51] (see Appendix A):

$$S_{21} = 1 - \frac{\kappa}{\kappa + \gamma} \frac{1 + i \tan\phi}{1 + 2i(\delta - \xi n)}, \tag{2}$$

where the frequency detuning is written in reduced form $\delta = \omega - \omega_0/\kappa + \gamma$, and $n = n_{ph}/\tilde{n}_{in}$ is a function of frequency and reduced circulating power $\xi = K[\kappa/hf\ (\kappa + \gamma)^3]P_{in}$. We plot steady-state transmission data taken near the bifurcation power in Fig. 4(a) along

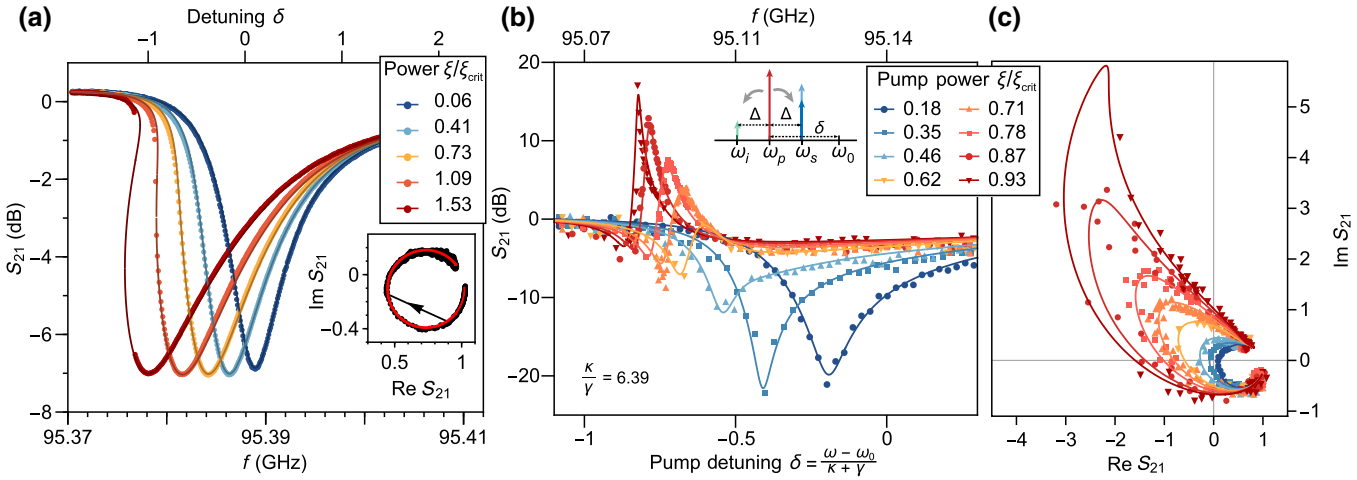

FIG. 4. Nonlinear response and four-wave mixing. (a) Transmission of a typical resonance at a range of powers near and above the bifurcation showing good agreement with a Kerr nonlinear response. The inset shows overlaid data and fits in the complex plane just below and above the bifurcation point. (b),(c) Parametric conversion gain with a 95.1-GHz device with the same film thickness as for (a) as a function of reduced pump frequency δ for a fixed signal detuning Δ of +450 kHz, taken at increasing pump powers. Solid lines correspond to the theoretical response. The initial forward deamplification is better understood when the response is viewed in the complex plane (c), where we observe smooth parametric deformation from the single-tone response.

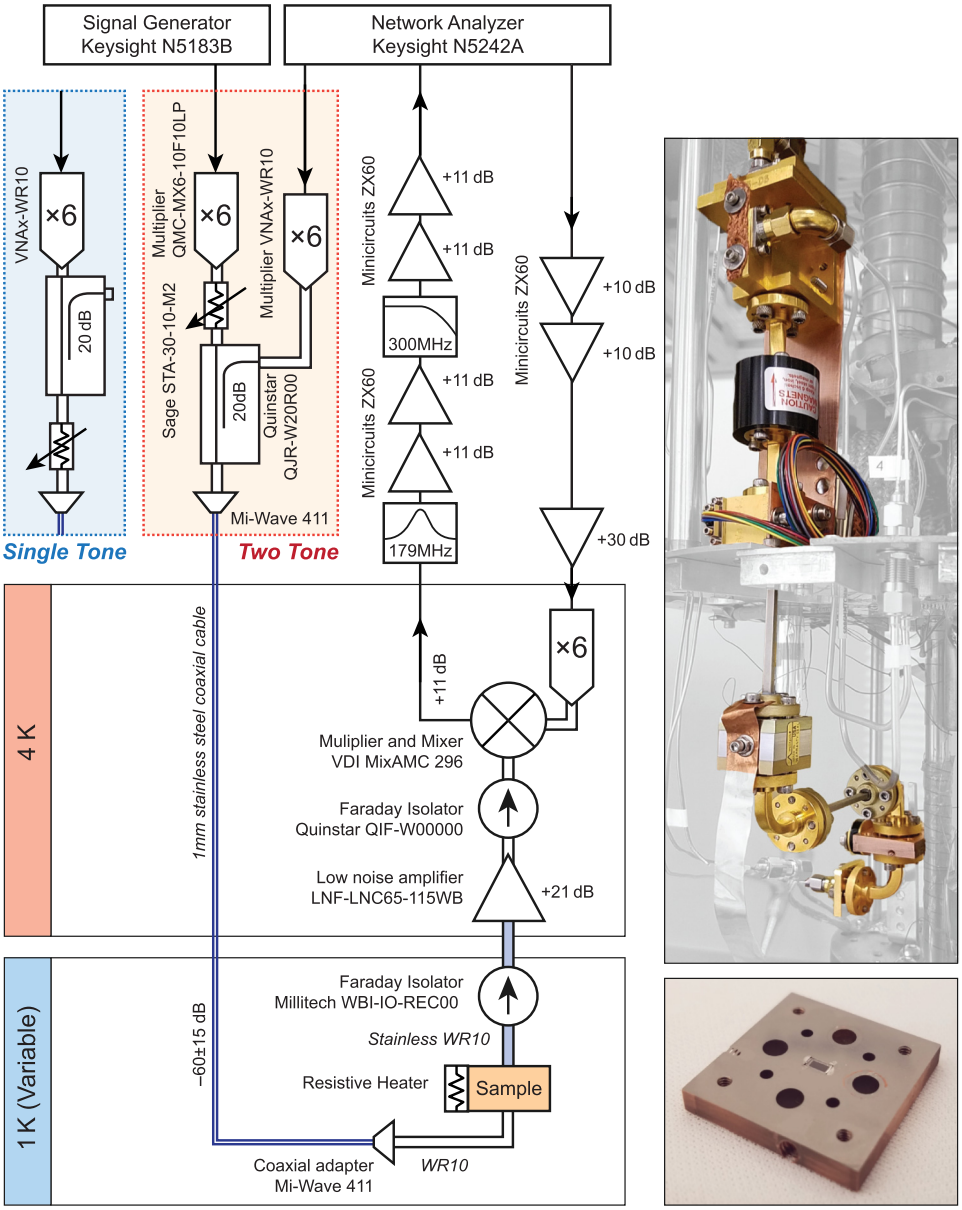

FIG. 5. Millimeter-wave measurement setup for single-tone and two-tone configurations. Colored tabs show temperature stages inside the ^{4}He adsorption refrigerator. The photograph at the top right highlights relevant hardware inside the fridge. The photograph at the bottom right shows the sample with the top waveguide removed.

with fits to Eq. (2), with system parameters κ, ϕ, and ω_0 constrained to low-power values and find the model to be in good agreement with measurements.

We further explore nonlinear dynamics by stimulating degenerate four-wave mixing with the addition of a continuous-wave classical pump (see Fig. 5).

When a high-power pump tone at ω_p is on resonance with the down-shifted resonance frequency, and a low-power signal at ω_s is at a frequency detuning Δ from the pump, we expect to observe the net conversion of two pump photons into a signal photon and an idler photon at their sum-average frequency [Fig. 4(b), inset]. This effect is most pronounced when all frequencies are within the resonant bandwidth, and the pump power ξ approaches the bifurcation point ξ_{crit}, but is limited by the loss fraction γ/κ. We measure the pump-signal conversion efficiency of a high-bandwidth, high-K device in the propagation direction as a function of reduced pump frequency δ for increasing pump powers ξ and a fixed signal power corresponding to $\bar{n}_{\mathrm{ph}} \simeq 9$ [Figs. 4(b) and 4(c)]. We find that this behavior is accurately captured with an analytical model (see Appendix A) based on the theoretical analysis in Refs. [44,50] and overlay the results. For increasing pump powers, we observe smooth parametric deformation from the single-tone response in the complex plane. For higher powers, we observe increasing gain with decreasing linewidth similar to what was reported in Refs. [50,52], up to a maximum measured forward efficiency of +16 dB. The slight curvature in the complex plane is a result of the finite pump-signal detuning Δ.

V. CONCLUSION

The demonstration of degenerate four-wave mixing realizes an important milestone for the development of quantum devices at millimeter-wave frequencies and temperatures above 1 K. For NbN films thicker than 25 nm, we measure millimeter-wave resonators with internal quality factors exceeding 2×10^4 at single-photon powers, and by reducing the wire width to 500 nm, we achieve self-Kerr-nonlinearities up to 1.21 kHz for linewidths ranging from 1 to 200 MHz. With some modification, the devices in this work could easily be redesigned as parametric amplifiers, which at microwave frequencies have been shown to achieve near-quantum-limited noise figures and quadrature squeezing [52–55]. While it is insufficient for implementation of a millimeter-wave artificial atom, the Kerr nonlinearity we measure arising from high-KI thin films can further be used for superinductors [33,56], photon frequency conversion [8], parametric mode cooling [57,58], phase-slip junctions [59,60], and mode squeezing [52] realized at millimeter-wave frequencies. This opens the door to a new generation of high-frequency quantum experiments at temperatures above 1 K.

ACKNOWLEDGMENTS

The authors thank P. Duda, P.S. Barry, and E. Shirokoff for assistance developing deposition recipes, as well as M. Wesson for supporting film characterization. We acknowledge useful discussions with S.J. Whiteley, and thank J. Jureller for assistance with the facilities of the University of Chicago Materials Research Science and Engineering Center. This work was supported by the Army Research Office under Grant No. W911NF-17-C-0024, partially supported by the University of Chicago Materials Research Science and Engineering Center, which is funded by the National Science Foundation under Grant No. DMR-1420709, and partially supported by the National Science Foundation Graduate Research Fellowship under Grant No. DGE-1746045. Devices were fabricated in the Pritzker Nanofabrication Facility at the University of Chicago, which receives support from the Soft and Hybrid Nanotechnology Experimental (SHyNE) Resource (Grant No. NSF ECCS-1542205).

APPENDIX A: KERR NONLINEAR DYNAMICS FOR A SIDE-COUPLED RESONATOR

Here we outline a simple method inspired by Refs. [61,62] to decompose a side-coupled resonator into a linear network containing a one-sided cavity, which is very well understood in the language of input-output theory used in quantum optics [63]. This allows us to map well-modeled dynamics of a Kerr nonlinear cavity driven in reflection [44,50] to a side-coupled resonator measured in transmission, obtaining results in agreement with the work reported in Ref. [51], which used a more direct approach.

On the basis of the circuit model in Fig. 1(d), and the argument that a symmetrically coupled resonator will radiate equally in both directions, we consider the three-port H-plane splitter. This lossless but unmatched network [64] has symmetric ports 1 and 2 corresponding to the transmission line, and matched port 3 leading to the single-port coupled resonator Z_R as shown in Fig. 6(a). [This system can also be described by a network consisting of a 50:50 beam splitter, a perfect mirror, and a $\pi/2$ phase shifter as shown in Fig. 6(b), which yields the same key results if we are careful to use correct boundary conditions]. If we place a black-box element on port 3, we can describe its input and output fields in terms of the waveguide input and

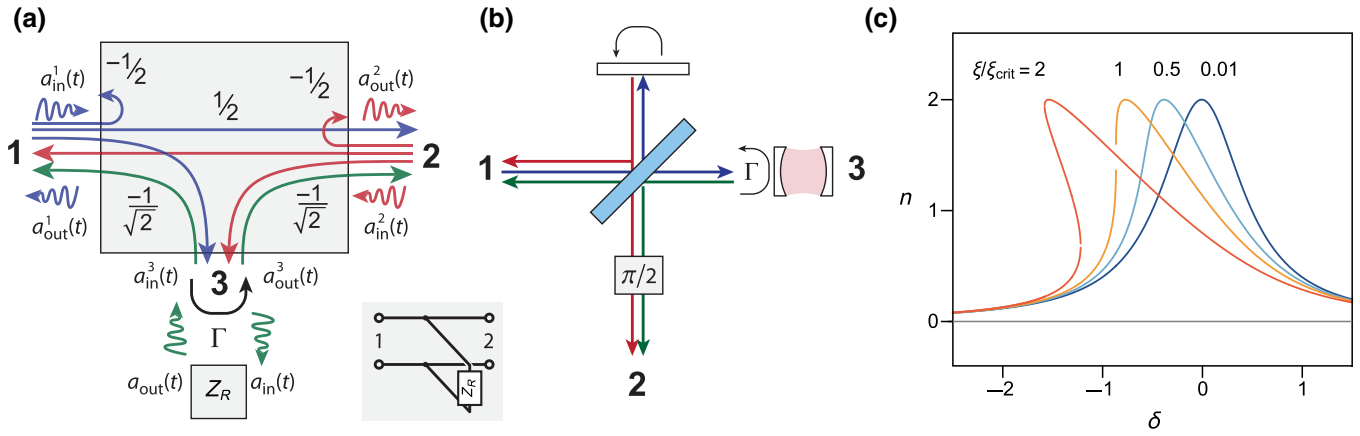

FIG. 6. Side-coupled resonator model. (a) Three-port network of an H-plane splitter coupled to a black-box resonator, showing corresponding transmission coefficients with input and output fields labeled by port. The inset shows the equivalent-circuit network. (b) Analogous configuration for an optical cavity, adjusted for boundary conditions. (c) Normalized photon number as a function of reduced pump frequency δ for reduced drive strengths ξ, where $\xi_{\text{crit}} = -2/\sqrt{27}$.

output fields:

$$\begin{pmatrix} a_{\rm in}(t) \\ a_{\rm out}(t) \end{pmatrix} = \frac{-1}{\sqrt{2}} \begin{pmatrix} a_1^{\rm in}(t) + a_2^{\rm in}(t) \\ a_1^{\rm out}(t) + a_2^{\rm out}(t) \end{pmatrix}. \tag{A1}$$

If we describe the black box with an arbitrary reflection term $\Gamma = a_{\rm out}(t)/a_{\rm in}(t)$, the scattering matrix of the system reduces to

$$S = \frac{1}{2} \begin{pmatrix} \Gamma - 1 & \Gamma + 1 \\ \Gamma + 1 & \Gamma - 1 \end{pmatrix}. \tag{A2}$$

We can now verify that far off resonance, for open-circuit perfect reflection $\Gamma \to 1$, we recover perfect transmission. With a map of waveguide inputs and outputs, we replace the black box with a Kerr nonlinear one-port coupled resonator, which has the steady-state condition [50,63]

$$i(\omega - \omega_0)a + \frac{\kappa + \gamma}{2}a - iK|a|^2 a^* = \sqrt{\kappa}a_{\rm in} = -\sqrt{\frac{\kappa}{2}}a_1^{\rm in}. \tag{A3}$$

We have been careful to use the microwave convention for Fourier transforms, and $n_{\rm ph} = |a|^2$ corresponds to the average number of photons in the resonator. Multiplying Eq. (A3) by its complex conjugate, we obtain an equation governing the normalized number of photons in the resonator n:

$$\left(\frac{1}{4} + \delta^2\right) n - 2\delta\xi n^2 + \xi^2 n^3 = \frac{1}{2} \tag{A4}$$

where similarly to Ref. [50], n, ξ, and δ are defined as

$$n = \frac{|a|^2}{|a_1^{\rm in}|^2}\frac{(\kappa + \gamma)^2}{\kappa}, \tag{A5}$$

$$\xi = \frac{|a_1^{\rm in}|^2 \kappa K}{(\kappa + \gamma)^3}, \tag{A6}$$

$$\delta = \frac{\omega - \omega_0}{\kappa + \gamma}. \tag{A7}$$

We plot n as a function of δ for various drive strengths ξ in Fig. 6(c), finding that n reaches a maximum value of 2. At the critical value $\xi_{\rm crit} = -2/\sqrt{27}$, Eq. (A4) has three real solutions, leading to the onset of bifurcation. On the basis of the resonator boundary conditions [65] $a_{\rm out} = a_{\rm in} + a\sqrt{\kappa}$ and Eq. (A3), the reflection coefficient Γ will be given by [44,50,63]

$$\Gamma = 1 - \frac{\kappa}{\kappa + \gamma}\frac{1}{\frac{1}{2} + i(\delta - \xi n)}. \tag{A8}$$

Far off resonance, an impedance mismatch on output port 2 results in nonzero reflection $|r| = \sin\phi$ and transmission $|t| = \cos\phi$ less than unity. To account for this while preserving the unitarity of the S matrix, we apply transformations of the form $e^{i\phi}$ to each path of the three-port network, yielding $S_{21} = (\Gamma e^{i\phi} + e^{-i\phi})/2$. Mapping Eq. (A8) to the modified three-port network, we obtain the result used in the main text, which in the respective limits agrees with Refs. [39,51]:

$$S_{21} = 1 - \frac{\kappa}{\kappa + \gamma}\frac{e^{i\phi}}{\cos\phi}\frac{1}{1 + 2i(\delta - \xi n)}. \tag{A9}$$

At low powers ($\xi n \to 0$), Eq. (A9) reduces to Eq. (1).

We follow a similar approach to obtain expressions for parametric conversion gain using the derived input-output relations to map the key results from Ref. [50] to the waveguide inputs and outputs. With use of microwave conventions for Fourier transforms, the one-port gain of a signal detuned from the pump by $+\Delta = \omega_s - \omega_p/\kappa + \gamma$ is given by

$$g_s = \frac{a_\Delta^{\rm out}}{a_\Delta^{\rm in}} = 1 - \frac{\kappa}{\kappa + \gamma}\frac{\frac{1}{2} - i(\delta - 2\xi n - \Delta)}{(i\Delta + \lambda_+)(i\Delta + \lambda_-)}, \tag{A10}$$

with $\lambda_\pm = \frac{1}{2} \pm \sqrt{(\xi n)^2 - (\delta - 2\xi n)^2}$. Use of the three-port-network transformations above yields the normalized forward (in the direction of propagation) signal gain:

$$g_s^+ = \frac{a_{2,\Delta}^{\rm out}}{a_{1,\Delta}^{\rm in}} = 1 - \frac{\kappa}{\kappa + \gamma}\frac{e^{i\phi}}{\cos\phi}\frac{\frac{1}{2} - i(\delta - 2\xi n - \Delta)}{2(i\Delta + \lambda_+)(i\Delta + \lambda_-)}. \tag{A11}$$

APPENDIX B: DEVICE FABRICATION

All devices are fabricated on (100 ± 25)-μm-thick C-plane (0001) sapphire wafers with a diameter of 50.8 mm. The wafers are cleaned with organic solvents (toluene, acetone, methanol, 2-propanol) and deionized (DI) water in an ultrasonic bath to remove contamination, and are then annealed at 1200 °C for 1.5 h. Before film deposition, the wafers undergo a second clean with organic solvents (toluene, acetone, methanol, 2-propanol) and DI water in an unltrasonic bath, followed by a 2-min clean in 50 °C Nano-Strip™ etch, and a rinse with high-purity DI water. The wafers then undergo a dehydration bake at 180 °C in air for 3 min.

Immediately afterward, the wafers are loaded into an Ultratech Fiji G2 plasma-enhanced-atomic-layer-deposition tool for metallization, where they first undergo a 1 h bake at 300 °C under a vacuum continuously purged with argon gas at 5 sccm. Chamber walls match the substrate temperature. The deposition parameters and machine configuration are adapted from Ref. [32]. (*t*-Butylimido)tris(diethylamido)niobium(V) (TBTDEN) is used as the niobium precursor, which is kept at 100 °C and

delivered by a precursor Boost^{TM} system, which introduces argon gas into the precursor cylinder to promote material transfer of the low-vapor-pressure precursor to the wafer [32]. The deposition cycle consists of three 0.5-s pulses of boosted TBTDEN followed by 40 s of 300-W plasma consisting of hydrogen at 80 sccm and nitrogen at 5 sccm. A flow of nitrogen at 5 sccm and argon at 10 sccm is maintained throughout the deposition process. After deposition, the wafer is allowed to passively cool to 250 °C under a vacuum.

Following deposition, the wafers are cleaned with DI water in an ultrasonic bath to remove particulates, and then undergo a dehydration bake at 180 °C in air for 3 min before being coated with resist. For optical lithography, to avoid defocusing from wafer deformation, the wafers are mounted to a silicon handle wafer with AZ MiR 703 photoresist cured at 115 °C. The wafers are then coated with approximately 1 μm of AZ MiR 703 positive I-line photoresist and exposed with a Heidelberg MLA150 direct writer. For electron-beam lithography, the wafers are first coated with approximately 200 nm of ARN 7520 negative resist, followed by 40 nm of Elektra AR PC 5090 conductive resist, and are then exposed with a Raith EBPG5000 Plus electron-beam writer. The conductive coating is removed by a 60-s DI-water quench. Both optical and electron-beam resists are baked at 110 °C to further harden the resist, and are then developed for 60 s in AZ MIF 300, followed by a 60-s quench in DI water. The rounded corners of our devices are by design to diffuse electric fields and reduce coupling to two-level systems, and are not defects induced by lithographic resolution.

The NbN films are etched in a Plasma-Therm inductively-coupled-plasma etcher. Etch chemistry, substrate etch depth, and etch time have been shown to affect planar-resonator quality factors [66], in particular due to the formation of cross-linked polymers at the metal-resist interface after the bulk metal has been etched away. For this reason we scale the sample etch times to metal thickness, with a fixed overetch time of 30 s to ensure complete metal removal. We use a fluorine-based ICP etch chemistry with a plasma consisting of SF_6 at 15 sccm , CHF_3 at 40 sccm, and Ar at 10 sccm. ICP and bias powers are kept at 100 W, and the substrate is cooled to 10 °C. Following etching, the resist is stripped in a combination of acetone and 80-°C Remover PG (*N*-methyl-2-pyrrolidone), which also serve to release the wafer from the silicon carrier wafer. The wafers are then cleaned with organic solvents (acetone, 2-propanol) and DI water, coated with an approximately-2-μm protective layer of photoresist, and diced into 3.3×2.3 mm^2 chips. These are stripped of protective resist with 80-°C Remover PG, cleaned with organic solvents (acetone, 2-propanol) and DI water, dried on an unpolished sapphire carrier wafer in air at 80 °C, and then mounted with indium wire in the copper box described in the main text.

APPENDIX C: FILM CHARACTERIZATION

Dc film-characterization measurements are performed with a Quantum Design physical property measurement system (PPMS) with a base temperature of 1.8 K. Test structures consisting of a 1.5 mm $\times$ 40 μm wire are patterned on 7×7 mm^2 chips undergoing the process described in Appendix B along with device wafers, and are then wirebonded for four-wire measurements. Finished structures are kept in a low, approximately-500-mTorr vacuum in an effort to minimize oxide growth before measurement, as we observe decreases up to 1 K in critical temperatures for samples aged for several days in air, likely a result of oxide growth [43] reducing the superconducting-film thickness.

After cooling the samples to 10 K (3 K in the case of the 8-nm film) in ambient magnetic fields, we verify that the residual resistance of the film drops below the instrument noise floor of around 5×10^{-3} Ω. After thermalization for 1 h, the samples are warmed up to 20 K at a rate of 0.1 K/min, and are then warmed to 300 K at a rate of 1 K/min. In Fig. 7(a) we plot measured resistivity as a function of temperature for the films in this study, which we use to extract T_c and ρ_n and calculate $R_\square$ and $L_\square$ for the films. Similarly to previous studies [33], resistivity decreases with temperature above the superconducting transition, which is typical for strongly disordered materials [33,38].

APPENDIX D: MILLIMETER-WAVE MEASUREMENT SETUP AND CALIBRATION

All millimeter-wave characterizations were performed in a custom-built ^{4}He adsorption refrigerator with a base

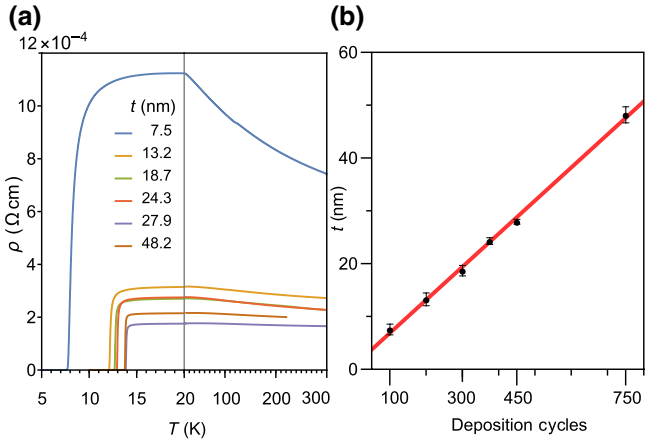

FIG. 7. Film measurements. (a) Measured resistivity as a function of temperature showing decreasing resistivity with increasing temperature above the superconducting transition characteristic of NbN. (b) Thicknesses measured by profilometry as a function of deposition cycles, with a linear fit overlaid in red. We extract a growth rate of 0.63 Å per cycle.

temperature of 0.9 K, and a cycle duration of 3 h. We generate millimeter-wave signals (75–115 GHz) at room temperature by sending microwave signals (12–19 GHz) into a frequency multiplier. We convert the generated waveguide TE_{10} mode to a coaxial mode in a 1-mm-diameter stainless steel and beryllium copper coaxial cable, which carries the signal to the 1-K stage of the fridge, with mechanical thermalization at each intermediate stage, and then convert the coaxial signal back to a WR10 waveguide, which leads to the device under test. The cables and waveguide-cable converters have a combined frequency-dependent loss ranging from 55.6 to 75.8 dB in the W band, which is dominated by the cable loss. We confirm the attenuation and incident device power at room temperature with a calibrated power meter (Agilent W8486A) and a referenced measurement with a VNAx805 receiver; however, cryogenic shifts in cable transmission and minute shifts in waveguide alignment likely result in small variations in transmitted power. We are able to further confirm the applied power by measuring the lowest observed bifurcation point, and find that most bifurcation powers agree with predictions, yielding a maximum combined power uncertainty of approximately ±5 dBm, which sets the uncertainty in our photon-number measurements.

The sample is isolated from both millimeter-wave and thermal radiation from the 4-K plate with two stainless steel waveguides 2 in. long and a Faraday isolator. Using a resistive heater and a standard-curve ruthenium oxide thermometer, we can perform temperature sweeps on the sample without significantly affecting the fridge-stage temperatures. A low-noise amplifier ($T_N \sim 28$ K) amplifies the signal before it passes through another Faraday isolator, which further blocks any leaking signals. The signal then passes to a cryogenic mixer, which converts the signal to radio waves (100–300 MHz), which we filter, amplify, and measure at room temperature with a network analyzer. We control the signal power by varying the input attenuation and multiplier input power, confirming the incident power at the sample with room-temperature calibrations as described above. For two-tone measurements, we move the signal path to the 20-dB port of the input directional coupler, and add an additional frequency multiplier fed by a reference-locked microwave signal generator. For single-tone measurements, the 20-dB port is capped with a short to minimize incident stray radiation.

APPENDIX E: BCS-CONDUCTIVITY TEMPERATURE DEPENDENCE

Because of the large kinetic inductance fraction α, or magnetic field participation ratio of the thin-film resonators, we expect higher sensitivity to loss from complex conductivity, which in turn is sensitive to temperature. In Fig. 8(a) we show the quality factor decrease as a function of temperature for resonators with four different thicknesses, with solid lines corresponding to a model of the form

$$Q_i(T)^{-1} = Q_{i,\max}^{-1} + Q_\sigma(T)^{-1}, \tag{E1}$$

where $Q_{i,\max}$ is a temperature-independent upper bound arising from other sources of loss, and the conduction loss Q_σ is given by [67]

$$Q_\sigma(T) = \frac{1}{\alpha}\frac{\sigma_2(T,T_c)}{\sigma_1(T,T_c)}, \tag{E2}$$

where σ_1 and σ_2 are the real and imaginary parts, respectively, of the complex surface impedance, which are calculated by numerically integrating the Mattis-Bardeen equations for σ_1/σ_n and σ_2/σ_n [67–69]. We use α and T_c as

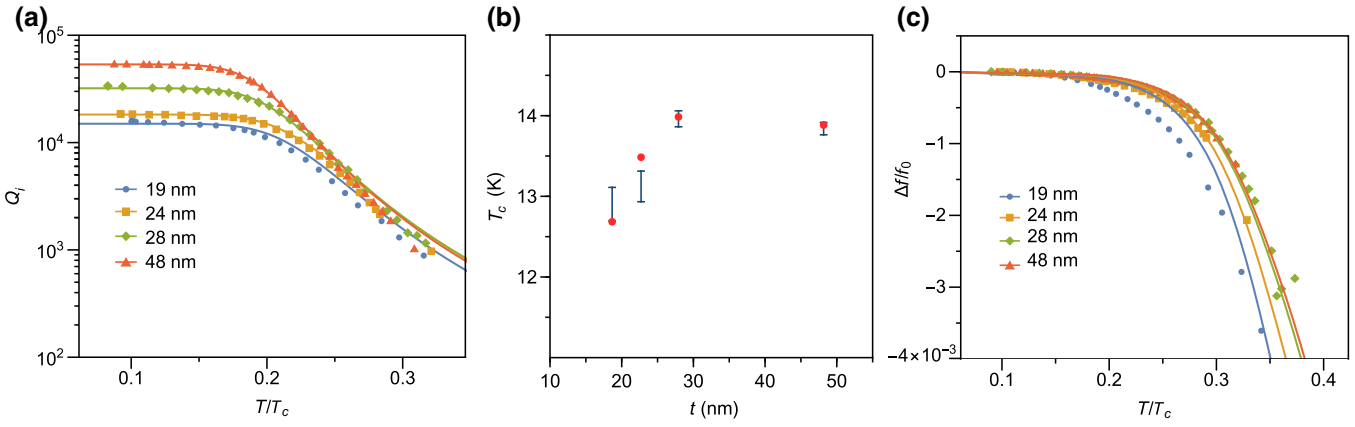

FIG. 8. Temperature dependence of BCS conductivity. (a) High-power Q_i as a function of normalized temperature for four resonators of different film thickness. Solid lines correspond to a BCS model with T_c and kinetic inductance fraction α as fit parameters. (b) Extracted T_c from fitting to the BCS model (red dots), compared with T_c from dc resistivity measurements. (c) Normalized frequency shift of the same resonators as a function of temperature, with overlaid predictions from the Mattis-Bardeen equations for σ_2/σ_n with parameters taken from fits in (a).

fit parameters in the model. Below 2 K ($T/T_c \sim 0.15$), Q_i saturates, which indicates that conduction loss does not limit Q_i for these devices. We note minor deviations from theory at higher temperatures, which may be a result of physical deviations from the standard-curve calibrations used for the ruthenium oxide thermometer. Since these resonators are fabricated with $Q_e > 10^4$, measuring resonators at higher temperatures where Q_i is below 10^3 proves experimentally challenging. In Fig. 8(b) we plot the fitted T_c values against those obtained with dc measurements and find reasonable agreement for greater-thickness films; however, the uncertainty in temperature calibration combined with the relatively low saturation values result in fitted T_c uncertainties of around 0.4 K.

Bardeen-Cooper-Schrieffer theory also predicts a shift in London length as a function of temperature, which in the dirty (high-disorder) limit is given by [68,70]

$$\frac{\lambda(T)}{\lambda(0)} = \frac{1}{\sqrt{\frac{\Delta(T)}{\Delta_0}\tanh\left(\frac{\Delta_0}{2k_bT}\right)}}. \tag{E3}$$

We can measure this by tracking the resonance-frequency shift. For sufficiently large kinetic inductance fractions, or $L_k \gg L_g$, the kinetic inductance will dominate the total inductance, so the normalized frequency shift will be given by [70]

$$\frac{f_0(T)}{f_0(0)} = \sqrt{\frac{\Delta(T)}{\Delta_0}\tanh\left(\frac{\Delta_0}{2k_bT}\right)}. \tag{E4}$$

Figure 8(c) shows the normalized frequency shift as a function of normalized temperature and predictions from Eq. (E4) with parameters α and T_c taken from fits to $Q_i(T)$ above. Notably, we find significant deviation from BCS theory for smaller thicknesses, which was previously observed for high-disorder films [25,31,70].

APPENDIX F: CONTROLLING NONLINEARITY IN THE PRESENCE OF ADDITIONAL LOSSES

From Ref. [44], we expect the self-Kerr-nonlinearity originating from kinetic inductance of a $\lambda/4$ resonator to be

$$K = -\frac{\hbar\omega_0^2}{I_c^2}\int_0^l dx u_0^4 \Delta L \propto -\frac{\hbar\omega_0^2 L_k}{J_c^2 w^2 t^2}, \tag{F1}$$

where in our case the nonlinear kinetic inductance ΔL is constant along the transmission line, so integrating over the fundamental mode profile u_0 yields a constant. We also transform the critical current I_c into a critical current density J_c, and use the assumption that the nonlinear kinetic inductance is proportional to the linear kinetic inductance [47,51]. Figure 9(a) expands on Fig. 3(b), showing measured self-Kerr-constants for all resonators in this study (grouped into points by film thickness and wire width) as a function of the parameters in Eq. (F1), with the solid line corresponding to a linear fit. We also add data from identical resonators fabricated from 30-nm electron-beam-evaporated niobium to extend the parameter range. We find reasonable agreement with dependence on the parameters in Eq. (F1); however, the dependence is much-less clear than that on wire width w.

Nonlinear kinetic inductance is also associated with a nonlinear resistance of the same form $R = R_0 + \Delta R I^2/I_c^2$.

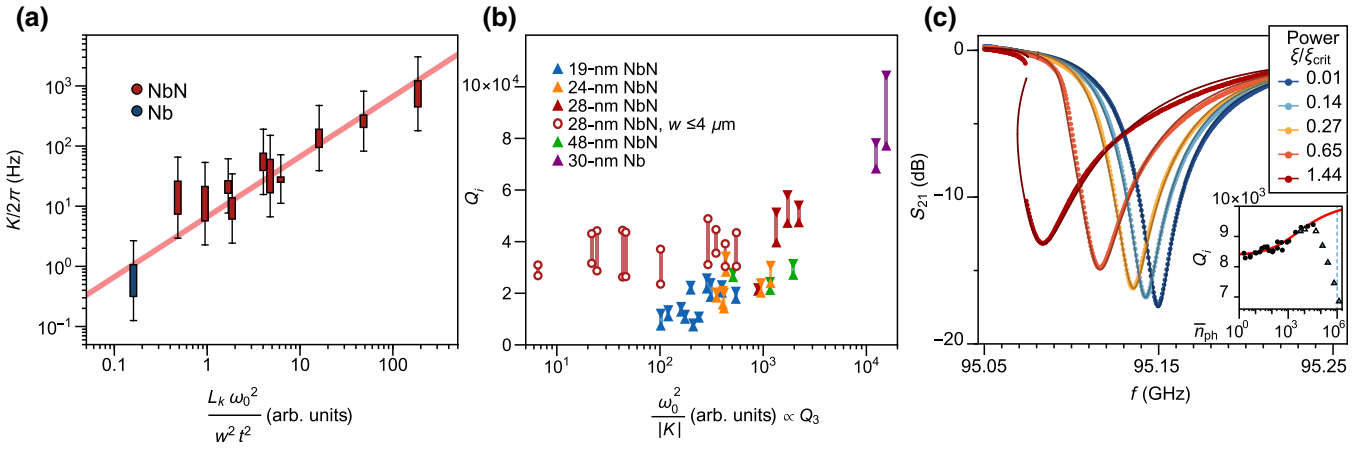

FIG. 9. (a) Self-Kerr-constant $|K_{00}|$ as a function of parameters in Eq. (F1), with a linear fit overlaid as a solid line. Solid bars correspond to value ranges for groups of similar film thicknesses and wire widths, with error bars marking systematic uncertainty. (b) Q_i as a function of $\omega_0^2/|K_{00}|$, which corresponds to the loss Q_3 associated with kinetic inductance. Points correspond to low-power and high-power limits of Q_i. Devices with differing wire width (empty circles) do not appear to be correlated with Q_3. (c) Transmission as a function of frequency for a 18.7-nm-thick device at 95.15 GHz taken at increasing powers ξ, with the inset highlighting decreasing Q_i near the bifurcation power $\xi_{\rm crit}$ (dashed blue line) deviating from the two-level-system loss model (red line). Triangles correspond to nonlinear model fits, with traces shown in the main panel marked in blue.

On the basis of Ref. [44], and assuming the nonlinear resistance scales with kinetic inductance, the losses associated with nonlinear resistance will be given by

$$\gamma_3 = \frac{\omega_0}{Q_3} = \frac{3\hbar\omega_0}{8I_c^2}\int_0^l dx u_0^4 \Delta R \propto \frac{\hbar\omega_0 L_k}{J_c^2 w^2 t^2} \sim \frac{-K}{\omega_0}. \quad \text{(F2)}$$

This indicates that upper bounds on nonlinear losses should scale as $Q_3 \sim \omega_0^2/|K|$. In Fig. 9(b) we plot low-power and high-power limits of the Q_i devices in this study with the addition of the 30-nm niobium devices described above, and find that for resonators with fixed wire widths $w = 4\ \mu$m, there appears to be a potential correlation of Q_i with Q_3, indicating nonlinear resistance may be a potential loss mechanism.

In our analysis, we also do not take into account higher harmonics of the resonator, which will be coupled to the fundamental mode by cross-Kerr-interactions χ_{mn}, which for evenly spaced harmonics scale as [44]

$$\chi_{mn} = -\frac{3\hbar\omega_m\omega_n}{I_c^2}\int_0^l dx u_m^2 u_n^2 \Delta L \propto K. \quad \text{(F3)}$$

Given the proportionality to K, the correlation described above may also potentially be a result of cross-Kerr-effects. For linewidths great enough to cover any deviations from evenly spaced higher harmonics, we anticipate that we will see power-dependent conversion processes: in particular, for a Kerr nonlinear system with harmonics spaced at ω_0 and $3\omega_0$, at powers approaching the critical power we would expect increased conversion efficiency from the fundamental to the third harmonic [71], which in our experiment would be observed as increased resonator loss at higher powers.

In Fig. 9(c) we show the atypical transmission spectra of a 18.7-nm-thick, 4-μm-wide device with a particularly large linewidth showing decreasing Q_i near the bifurcation power (above $n_{\mathrm{ph}} \sim 10^5$), departing from the two-level-system model described in the main text. This additional power-dependent loss may be the result of the nonlinear mechanisms described above, but may also be a result of circulating currents exceeding the thin-film critical current density, which is lowered by the increased London lengths of the thinner films [72,73]. However, since the loss could also simply be a result of frequency-dependent dissipation, the source remains unclear.

In Fig. 9(b), we also observe that resonators achieving higher nonlinearities by reduction of the wire width do not appear to be affected by the nonlinear loss rate described above. We also find that these devices do not show obvious signs of the high-power loss shown in Fig. 9(c). While this may be a result of the difference in fabrication methods (see Appendix B), the thinner wires may have higher vortex critical fields [74], leading to reduced vortex formation, and thus lower loss associated with vortex dissipation. Additionally, the thinner wires at the shorted end of the quarter-wave section of the resonator further shift the higher harmonics, potentially resulting in lower cross-Kerr-conversion loss.

[1] Michel H. Devoret and Robert J. Schoelkopf, Superconducting circuits for quantum information: An outlook, Science **339**, 1169 (2013).

[2] Alex I. Braginski, Superconductor electronics: Status and outlook, J. Supercond. Novel Magn. **32**, 23 (2019).

[3] Ze-Liang Xiang, Sahel Ashhab, J. Q. You, and Franco Nori, Hybrid quantum circuits: Superconducting circuits interacting with other quantum systems, Rev. Mod. Phys. **85**, 623 (2013).

[4] John J. L. Morton and Brendon W. Lovett, Hybrid solid-state qubits: The powerful role of electron spins, Annu. Rev. Condens. Matter Phys. **2**, 189 (2011).

[5] Sergei Vasilyev, Jarno Järvinen, Esa Tjukanoff, Alexander Kharitonov, and Simo Jaakkola, Cryogenic 2 mm wave electron spin resonance spectrometer with application to atomic hydrogen gas below 100 mk, Rev. Sci. Instrum. **75**, 94 (2004).

[6] Nabeel Aslam, Matthias Pfender, Rainer Stöhr, Philipp Neumann, Marc Scheffler, Hitoshi Sumiya, Hiroshi Abe, Shinobu Onoda, Takeshi Ohshima, Junichi Isoya *et al.*, Single spin optically detected magnetic resonance with 60–90 ghz (e-band) microwave resonators, Rev. Sci. Instrum. **86**, 064704 (2015).

[7] Jean-Michel Raimond, M. Brune, and Serge Haroche, Manipulating quantum entanglement with atoms and photons in a cavity, Rev. Mod. Phys. **73**, 565 (2001).

[8] Marek Pechal and Amir H. Safavi-Naeini, Millimeter-wave interconnects for microwave-frequency quantum machines, Phys. Rev. A **96**, 042305 (2017).

[9] John R. Tucker and Marc J. Feldman, Quantum detection at millimeter wavelengths, Rev. Mod. Phys. **57**, 1055 (1985).

[10] Yong Niu, Yong Li, Depeng Jin, Li Su, and Athanasios V. Vasilakos, A survey of millimeter wave communications (mmwave) for 5g: Opportunities and challenges, Wireless Netw. **21**, 2657 (2015).

[11] Maurizio Bozzi, Anthimos Georgiadis, and Kaijie Wu, Review of substrate-integrated waveguide circuits and antennas, IET Microwaves Antennas Propag. **5**, 909 (2011).

[12] C. L. Chang, P. A. R. Ade, Z. Ahmed, S. W. Allen, K. Arnold, J. E. Austermann, A. N. Bender, L. E. Bleem, B. A. Benson, J. E. Carlstrom *et al.*, Low loss superconducting microstrip development at argonne national lab, IEEE Trans. Appl. Supercond. **25**, 1 (2014).

[13] Ari David Brown, Emily M. Barrentine, Samuel H. Moseley, Omid Noroozian, and Thomas Stevenson, The impact of standard semiconductor fabrication processes on polycrystalline Nb thin-film surfaces, IEEE Trans. Appl. Supercond. **27**, 1 (2016).

[14] C. H. Zhang, J. B. Wu, B. B. Jin, Z. M. Ji, L. Kang, W. W. Xu, J. Chen, M. Tonouchi, and P. H. Wu, Low-loss terahertz metamaterial from superconducting niobium nitride films, Opt. Express **20**, 42 (2012).

[15] William J. Otter, Stephen M. Hanham, and Nick M. Ridler, 100 ghz ultra-high q-factor photonic crystal resonators, Nature **425**, 944 (2003).

[16] Stefan Kuhr, Sébastien Gleyzes, Christine Guerlin, Julien Bernu, U. Busk Hoff, Samuel Deléglise, Stefano Osnaghi, Michel Brune, J.-M. Raimond, Serge Haroche *et al.*, Ultra-high finesse Fabry-Pérot superconducting resonator, Appl. Phys. Lett. **90**, 164101 (2007).

[17] Erik Shirokoff, Peter S. Barry, Charles M. Bradford, Goutam Chattopadhyay, Peter Day, Simon Doyle, Steve Hailey-Dunsheath, Matthew I. Hollister, Attila Kovács, Christopher McKenney *et al.*, in *Millimeter, Submillimeter, and Far-Infrared Detectors and Instrumentation for Astronomy VI* (International Society for Optics and Photonics, Amsterdam, 2012), Vol. 8452, p. 84520R.

[18] A. Endo, C. Sfiligoj, S. J. C. Yates, J. J. A. Baselmans, D. J. Thoen, S. M. H. Javadzadeh, P. P. Van der Werf, A. M. Baryshev, and T. M. Klapwijk, On-chip filter bank spectroscopy at 600–700 ghz using nbtin superconducting resonators, Appl. Phys. Lett. **103**, 032601 (2013).

[19] Jiansong Gao, Anastasios Vayonakis, Omid Noroozian, Jonas Zmuidzinas, Peter K. Day, and Henry G. Leduc, in *AIP Conference Proceedings* (AIP, Melville, NY, 2009), Vol. 1185, pp. 164–167.

[20] U. Kongpop, Ari D. Brown, Samuel H. Moseley, Omid Noroozian, Edward J. Wollack *et al.*, A cryogenic waveguide mount for microstrip circuit and material characterization, IEEE Trans. Appl. Supercond. **27**, 1 (2017).

[21] Anthony R. Kerr, S.-K. Pan, Stéphane M. X. Claude, Philip Dindo, Arthur W. Lichtenberger, and Eugene F. Lauria, in *2013 IEEE MTT-S International Microwave Symposium Digest (MTT)* (IEEE, Seattle, WA, 2013), pp. 1–4.

[22] C. A. Mears, Qing Hu, P. L. Richards, A. H. Worsham, D. E. Prober, and A. V. Räisänen, Quantum-limited heterodyne detection of millimeter waves using superconducting tantalum tunnel junctions, Appl. Phys. Lett. **57**, 2487 (1990).

[23] A. Grimm, S. Jebari, D. Hazra, F. Blanchet, F. Gustavo, J. L. Thomassin, and M. Hofheinz, A self-aligned nanofabrication process for vertical NbN–MgO–NbN Josephson junctions, Supercond. Sci. Technol. **30**, 105002 (2017).

[24] David Olaya, Manuel Castellanos-Beltran, Javier F. Pulecio, John Biesecker, Soroush Khadem, Theodore Lewitt, Peter Hopkins, Paul Dresselhaus, and Samuel Benz, Planarized process for single-flux-quantum circuits with self-shunted $Nb/Nb_xSi_{1-x}/Nb$ Josephson junctions, IEEE Trans. Appl. Supercond. **29**, 1 (2019).

[25] Abigail Shearrow, Gerwin Koolstra, Samuel J. Whiteley, Nathan Earnest, Peter S. Barry, F. Joseph Heremans, David D. Awschalom, Erik Shirokoff, and David I. Schuster, Atomic layer deposition of titanium nitride for quantum circuits, Appl. Phys. Lett. **113**, 212601 (2018).

[26] N. Samkharadze, A. Bruno, P. Scarlino, G. Zheng, D. P. DiVincenzo, L. DiCarlo, and L. M. K. Vandersypen, High-Kinetic-Inductance Superconducting Nanowire Resonators for Circuit QED in a Magnetic Field, Phys. Rev. Appl. **5**, 044004 (2016).

[27] S. Hailey-Dunsheath, P. S. Barry, C. M. Bradford, G. Chattopadhyay, P. Day, S. Doyle, M. Hollister, A. Kovacs, H. G. LeDuc, N. Llombart *et al.*, Optical measurements of superspec: A millimeter-wave on-chip spectrometer, J. Low Temp. Phys. **176**, 841 (2014).

[28] Omid Noroozian, Emily Barrentine, Ari Brown, Giuseppe Cataldo, Negar Ehsan, Wen-Ting Hsieh, Thomas Stevenson, Kongpop U-yen, Edward Wollack, and Samuel Harvey Moseley, in *26TH International Symposium on Space Terahertz Technology* (Curran Associates, Inc, Cambridge, MA, 2015).

[29] Yachin Ivry, Chung-Soo Kim, Andrew E. Dane, Domenico De Fazio, Adam N. McCaughan, Kristen A. Sunter, Qingyuan Zhao, and Karl K. Berggren, Universal scaling of the critical temperature for thin films near the superconducting-to-insulating transition, Phys. Rev. B **90**, 214515 (2014).

[30] Anand Kamlapure, Mintu Mondal, Madhavi Chand, Archana Mishra, John Jesudasan, Vivas Bagwe, L. Benfatto, Vikram Tripathi, and Pratap Raychaudhuri, Measurement of magnetic penetration depth and superconducting energy gap in very thin epitaxial NbN films, Appl. Phys. Lett. **96**, 072509 (2010).

[31] Melissa R. Beebe, Douglas B. Beringer, Matthew C. Burton, Kaida Yang, and R. Alejandra Lukaszew, Stoichiometry and thickness dependence of superconducting properties of niobium nitride thin films, J. Vac. Sci. Technol. A: Vacuum Surfaces Films **34**, 021510 (2016).

[32] Mark J. Sowa, Yonas Yemane, Jinsong Zhang, Johanna C. Palmstrom, Ling Ju, Nicholas C. Strandwitz, Fritz B. Prinz, and J. Provine, Plasma-enhanced atomic layer deposition of superconducting niobium nitride, J. Vac. Sci. Technol. A: Vacuum Surfaces Films **35**, 01B143 (2017).

[33] David Niepce, Jonathan Burnett, and Jonas Bylander, High Kinetic Inductance NbN Nanowire Superinductors, Phys. Rev. Appl. **11**, 044014 (2019).

[34] Keiji Yoshida, Mohammad Sajjad Hossain, Takanobu Kisu, Keiji Enpuku, and Kaoru Yamafuji, Modeling of kinetic-inductance coplanar striplin with NbN thin films, Jpn. J. Appl. Phys. **31**, 3844 (1992).

[35] M. A. Skvortsov and M. V. Feigel'man, Superconductivity in Disordered Thin Films: Giant Mesoscopic Fluctuations, Phys. Rev. Lett. **95**, 057002 (2005).

[36] E. F. C. Driessen, P. C. J. J. Coumou, R. R. Tromp, P. J. De Visser, and T. M. Klapwijk, Strongly Disordered TiN and NbTiN s-Wave Superconductors Probed by Microwave Electrodynamics, Phys. Rev. Lett. **109**, 107003 (2012).

[37] J. E. Mooij, in *Nato Asi Series* (Plenum Press, New York, 1984), p. 325.

[38] Mintu Mondal, Anand Kamlapure, Madhavi Chand, Garima Saraswat, Sanjeev Kumar, John Jesudasan, L. Benfatto, Vikram Tripathi, and Pratap Raychaudhuri, Phase Fluctuations in a Strongly Disordered s-Wave NbN Superconductor Close to the Metal-Insulator Transition, Phys. Rev. Lett. **106**, 047001 (2011).

[39] M. S. Khalil, M. J. A. Stoutimore, F. C. Wellstood, and K. D. Osborn, An analysis method for asymmetric resonator transmission applied to superconducting devices, J. Appl. Phys. **111**, 054510 (2012).

[40] Anthony Megrant, Charles Neill, Rami Barends, Ben Chiaro, Yu Chen, Ludwig Feigl, Julian Kelly, Erik Lucero, Matteo Mariantoni, Peter J. J. O'Malley *et al.*,

Planar superconducting resonators with internal quality factors above one million, Appl. Phys. Lett. **100**, 113510 (2012).

[41] Jeremy M. Sage, Vladimir Bolkhovsky, William D. Oliver, Benjamin Turek, and Paul B. Welander, Study of loss in superconducting coplanar waveguide resonators, J. Appl. Phys. **109**, 063915 (2011).

[42] H. Wang, M. Hofheinz, J. Wenner, M. Ansmann, R. C. Bialczak, M. Lenander, Erik Lucero, M. Neeley, A. D. O'Connell, D. Sank *et al.*, Improving the coherence time of superconducting coplanar resonators, Appl. Phys. Lett. **95**, 233508 (2009).

[43] Owen Medeiros, Marco Colangelo, Ilya Charaev, and Karl K. Berggren, Measuring thickness in thin NbN films for superconducting devices, J. Vac. Sci. Technol. A: Vacuum Surfaces Films **37**, 041501 (2019).

[44] Bernard Yurke and Eyal Buks, Performance of cavity-parametric amplifiers, employing Kerr nonlinearites, in the presence of two-photon loss, J. Lightwave Technol. **24**, 5054 (2006).

[45] Ibrahim Nsanzineza, Ph.D. thesis, Syracuse University, 2016.

[46] J. Kitaygorsky, I. Komissarov, A. Jukna, D. Pan, O. Minaeva, N. Kaurova, A. Divochiy, A. Korneev, M. Tarkhov, B. Voronov *et al.*, Dark counts in nanostructured nbn superconducting single-photon detectors and bridges, IEEE Trans. Appl. Supercond. **17**, 275 (2007).

[47] Aditya Shreyas Kher, Ph.D. thesis, California Institute of Technology, 2017.

[48] The point diametrically opposite $S_{21} = 1$.

[49] Nataliya Maleeva, Lukas Grünhaupt, T. Klein, F. Levy-Bertrand, O. Dupre, M. Calvo, F. Valenti, P. Winkel, F. Friedrich, W. Wernsdorfer *et al.*, Circuit quantum electrodynamics of granular aluminum resonators, Nat. Commun. **9**, 3889 (2018).

[50] Christopher Eichler and Andreas Wallraff, Controlling the dynamic range of a Josephson parametric amplifier, EPJ Quantum Technol. **1**, 2 (2014).

[51] L. J. Swenson, P. K. Day, B. H. Eom, H. G. Leduc, N. Llombart, C. M. McKenney, O. Noroozian, and J. Zmuidzinas, Operation of a titanium nitride superconducting microresonator detector in the nonlinear regime, J. Appl. Phys. **113**, 104501 (2013).

[52] Erik A. Tholén, Adem Ergül, Evelyn M. Doherty, Frank M. Weber, Fabien Grégis, and David B. Haviland, Nonlinearities and parametric amplification in superconducting coplanar waveguide resonators, Appl. Phys. Lett. **90**, 253509 (2007).

[53] Byeong Ho Eom, Peter K. Day, Henry G. LeDuc, and Jonas Zmuidzinas, A wideband, low-noise superconducting amplifier with high dynamic range, Nat. Phys. **8**, 623 (2012).

[54] B. Yurke, Squeezed-state generation using a josephson parametric amplifier, JOSA B **4**, 1551 (1987).

[55] R. Movshovich, B. Yurke, P. G. Kaminsky, A. D. Smith, A. H. Silver, R. W. Simon, and M. V. Schneider, Observation of Zero-Point Noise Squeezing via a Josephson-Parametric Amplifier, Phys. Rev. Lett. **65**, 1419 (1990).

[56] M. T. Bell, I. A. Sadovskyy, L. B. Ioffe, A. Yu Kitaev, and M. E. Gershenson, Quantum Superinductor with Tunable Nonlinearity, Phys. Rev. Lett. **109**, 137003 (2012).

[57] Raphaël Khan, F. Massel, and T. T. Heikkilä, Cross-Kerr nonlinearity in optomechanical systems, Phys. Rev. A **91**, 043822 (2015).

[58] Jian-Song Zhang, Wei Zeng, and Ai-Xi Chen, Effects of cross-Kerr coupling and parametric nonlinearity on normal mode splitting, cooling, and entanglement in optomechanical systems, Quantum Inf. Process. **16**, 163 (2017).

[59] J. E. Mooij and Yu. V. Nazarov, Superconducting nanowires as quantum phase-slip junctions, Nat. Phys. **2**, 169 (2006).

[60] O. V. Astafiev, L. B. Ioffe, S. Kafanov, Yu. A. Pashkin, K. Yu Arutyunov, D. Shahar, O. Cohen, and J. S. Tsai, Coherent quantum phase slip, Nature **484**, 355 (2012).

[61] Benjamin A. Mazin, Ph.D. thesis, California Institute of Technology, 2005.

[62] Jiansong Gao, Ph.D. thesis, California Institute of Technology, 2008.

[63] Daniel F. Walls and Gerard J. Milburn, *Quantum Optics* (Springer Science & Business Media, Berlin, 2007).

[64] David M. Pozar, *Microwave Engineering* (John Wiley & Sons, New York, 2009).

[65] Alessandro Ridolfo, Martin Leib, Salvatore Savasta, and Michael J. Hartmann, Photon Blockade in the Ultrastrong Coupling Regime, Phys. Rev. Lett. **109**, 193602 (2012).

[66] Evgeniya H. Lock, Peng Xu, Timothy Kohler, Lizmarie Camacho, Joseph Prestigiacomo, Yaniv J. Rosen, and Kevin D. Osborn, Using surface engineering to modulate superconducting coplanar microwave resonator performance, IEEE Trans. Appl. Supercond. **29**, 1 (2019).

[67] Matthew James Reagor, Ph.D. thesis, Yale University, 2016.

[68] Michael Tinkham, *Introduction to Superconductivity* (McGraw-Hill, New York, 1975).

[69] D. C. Mattis and John Bardeen, Theory of the anomalous skin effect in normal and superconducting metals, Phys. Rev. **111**, 412 (1958).

[70] D. Hazra, S. Jebari, R. Albert, F. Blanchet, A. Grimm, C. Chapelier, and M. Hofheinz, Microwave response and electrical transport studies of disordered s wave superconductor: NbN thin films, arXiv:1806.03935 (2018).

[71] Hila Hashemi, Alejandro W. Rodriguez, J. D. Joannopoulos, Marin Soljačić, and Steven G. Johnson, Nonlinear harmonic generation and devices in doubly resonant Kerr cavities, Phys. Rev. A **79**, 013812 (2009).

[72] Evgeny F. Talantsev and Jeffery L. Tallon, Universal self-field critical current for thin-film superconductors, Nat. Commun. **6**, 7820 (2015).

[73] Osami Tsukamoto, AC losses in a type II superconductor strip with inhomogeneous critical current distribution, Supercond. Sci. Technol. **18**, 596 (2005).

[74] Gheorghe Stan, Stuart B. Field, and John M. Martinis, Critical Field for Complete Vortex Expulsion from Narrow Superconducting Strips, Phys. Rev. Lett. **92**, 097003 (2004).